CrossMark

MR-conditional steerable needle robot for intracerebral hemorrhage removal

Yue Chen[1] · Isuru S. Godage[2] · Saikat Sengupta[3] · Cindy Lin Liu[5] · Kyle D. Weaver[4] · Eric J. Barth[5]

Abstract

Background Intracerebral hemorrhage (ICH) is one of the deadliest forms of stroke in the USA. Conventional surgical techniques such as craniotomy or stereotactic aspiration disrupt a large volume of healthy brain tissue in their attempts to reach the surgical site. Consequently, the surviving patients suffer from debilitating complications.

Methods We fabricated a novel MR-conditional steerable needle robot for ICH treatment. The robot system is powered by a custom-designed high power and low-cost pneumatic motor. We tested the robot's targeting accuracy and MR-conditionality performance, and performed phantom evacuation experiment under MR image guidance.

Results Experiments demonstrate that the robotic hardware is MR-conditional; the robot has the targeting accuracy of 1.26 ± 1.22 mm in bench-top tests. With real-time MRI guidance, the robot successfully reached the desired target and evacuated an 11.3 ml phantom hematoma in 9 min.

Conclusion MRI-guided steerable needle robotic system is a potentially feasible approach for ICH treatment by providing accurate needle guidance and intraoperative surgical outcome evaluation.

Keywords Steerable needle robot · MRI · Intracerebral hemorrhage

Introduction

Intracerebral hemorrhage (ICH) is a life-threatening condition, and it accounts for 10–15% of all the stroke cases [1]. ICH occurs when a blood vessel in the brain ruptures and forms a pool of semi-clotted blood called the hematoma. It can rapidly compress the surrounding brain tissue and cause death or permanent damage, making it a leading contributor of serious long-term disability in the USA. Healthy brain tissue damage and mortality rate could be reduced by relieving the excess pressure generated by the hematoma [2]. Tradi-

tional surgical approaches to remove a hematoma and drugs have not been effective in reducing the overall mortality rate, and there remains no clinically proven effective treatment for the majority of ICH patients [3]. Furthermore, the literature reviews indicate that there is no obvious benefit of standard open surgical treatments over "watchful waiting," despite the fact that it could decompress the brain [4]. It has been hypothesized that this is due to the substantial volume of healthy brain tissue that needs to be disturbed to reach the hematoma in the conventional surgeries. High incidence, mortality, and long-term disability rates along with the invasive nature of surgical interventions, lack of widespread, reliable, and effective treatment of ICH provide the basic motivations to develop a safe minimally invasive approach to treat this disease.

Recent studies conducted on phantom models have shown that a concentric tube robot made from curved, superelastic tubes can reach a hemorrhagic site through a needle-sized (diameter ≤ 3 mm) path to successfully aspirate the hematoma from within [5]. These nested tubes enable reaching the hemorrhagic site following a straight trajectory and returning to the pre-curved shape within the hematoma to cover a larger workspace when extending from one another

✉ Yue Chen
  yc039@uark.edu

1 Department of Mechanical Engineering, University of Arkansas, Fayetteville, AR, USA

2 School of Computing, DePaul University, Chicago, IL, USA

3 Department of Radiology and Radiological Sciences, Vanderbilt University, Nashville, TN, USA

4 Department of Neurological Surgery, Vanderbilt Medical Center, Nashville, TN, USA

5 Department of Mechanical Engineering, Vanderbilt University, Nashville, TN, USA

[6]. This approach has the potential to decompress the brain with far less disruption while reaching the hematoma. Initial experiments conducted under computed tomography (CT) guidance showed that 83–92% of the hematoma can be successfully evacuated through this needle-sized treatment [5]. However, due to brain tissue elasticity, surrounding healthy tissue can fill the cavity during the aspiration process and cause significant brain shift and deformation. Hence, concentric tube robot-based ICH aspiration, guided by preoperative static CT images, carries a high risk of damaging healthy brain tissue during the aspiration process. Therefore, accurate intraoperative monitoring of hematoma-brain boundary is necessary for the proposed concentric tube robot-based minimally invasive treatment.

With the periodic intraoperative CT image feedback (4–5 scans per procedure), the safety and efficacy of the proposed procedure was significantly improved compared to the one with purely preoperative image guidance [7]. However, CT also has the drawback of exposing patients to ionizing radiation, providing low soft tissue contrast, as well as creating only intermittent images rather than real-time information. Mechanical patient-specific brain tissue deformation modeling has been suggested to predict the brain deformation during aspiration between consecutive CT imaging as a way to reduce the number of intraoperative CT images [8]. However, it is unable to capture the complex, highly dynamic viscoelastic interactions between brain and hematoma during continual removal and requires further development and validation.

The purpose of this paper is to propose MRI as an alternative imaging modality for CT in ICH aspiration guidance. Support for this idea comes from previous studies showing that MRI is equally or potentially even more accurate in diagnostic imaging of ICH [9] and providing better imaging of surrounding brain structures [10]. Furthermore, there is a desire for rapid intraoperative, multi-planar imaging during ICH aspiration [7], which has previously required a careful trade-off between image update frequency and ionizing radiation delivered during imaging. Recent advances in MRI real-time imaging (update rate: 1–2 Hz) enable intraoperative monitoring of the surgical tool position, tissue deformation, and surgical outcome [11–16]. Based on this, there is ample motivation to develop MRI-guided approaches for ICH aspiration despite the challenges of building robotic systems that are MRI conditional. To date, Masamune et al. [17] proposed 6 degrees of freedom (DoF) MR-conditional needle insertion robot for brain biopsy procedure in 1995. Sutherland et al. designed neuroArm MR-conditional robotic platform for neuro-microsurgeries [18]. Sheng et al. [19] presented a neurosurgical intracerebral hemorrhage evacuation (NICHE) robot in 2015, but no MR tests were performed. Su et al. [20] proposed a concentric tube continuum robot driven with

piezoelectric actuation for MRI-guided closed-loop targeting applications in 2016.

In this paper, we developed an MR-conditional ICH robot actuated by three custom-designed pneumatic motors that could accurately deploy the surgical tools toward the hemorrhage site under MRI guidance. The results presented here are the extensions of our recent conference abstract publication [21], with significant contributions on the aiming device design, robot kinematic modeling, real-time MR-guided needle insertion, and MR-guided ICH evacuation. This paper is arranged as follows. "Materials and methods" section presents the working principle of the aiming device and ICH robot design. "Results" section describes the experimental results of the proposed robot in bench-top tests and MR-guided phantom studies followed by the discussions in final section.

Materials and methods

Design overview

From the aforementioned discussion, the MR-guided ICH robotic evacuation procedure can be divided into two subtasks: (1) deploying the concentric tube robot into the hematoma at the predefined entry path and (2) steering the curved inner tube within the hematoma to perform the aspiration. Based on this task decomposition, the MR-guided ICH robot system includes two main mechanical modules, namely an aiming system and a concentric tube robot actuation unit (Fig. 1). The overall system design and construction are gov-
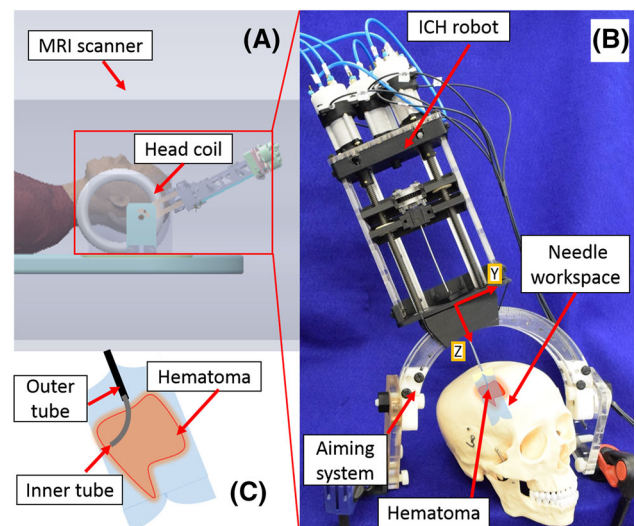

Fig. 1 a Schematic diagram of MR-conditional ICH robotic system in a 3T MRI scanner, **b** the ICH concentric tube robot with the custom-designed aiming device, **c** schematic diagram when the concentric tube inside the hematoma
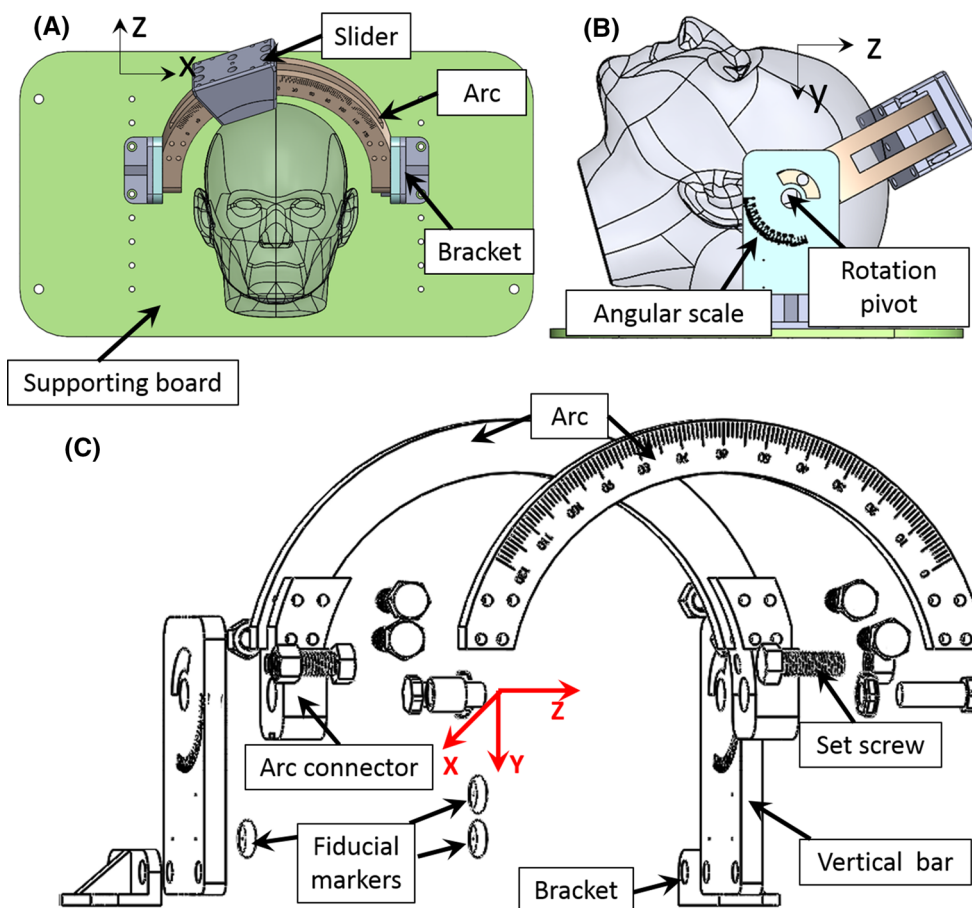
Fig. 2 Top view (**a**) and side view (**b**) of the 2-DoF aiming device attached to the skull model, **c** exploded view of the custom-designed aiming device. The yaw and roll DoF provide the entry angle of ICH robot. The coordinate frame in **a**, **b** indicates the MR frame, while the coordinate frame in **c** indicates the aiming device frame

erned by two main physical constraints: (1) the limited space and (2) strong magnetic field strength within an MRI scanner. In this study, a closed bore MRI scanner with 60 cm diameter was considered for the design of the proposed ICH robotic system so that it would fit within the majority of currently used 3T MRI scanner. The proposed robotic platform has the maximum height of 277 mm and the minimum height of 100 mm when the robot operates within its workspace. The robotic system should be conditional in a given MRI environment with a specified condition according to the American Society for Testing and Materials (ASTM) standard F2503 [22].

MR-conditional aiming device design

Figure 2 shows a schematic diagram of the human skull model with a custom-designed aiming device, which was developed based on the simplified 2-DoF Leksell stereotactic frame. To enable the proposed ICH aspiration procedure, the following mechanical modifications were introduced in the

aiming device compared to the conventional Leksell frame. First, the space between the aiming device and patient's head is increased to provide sufficient space for the placement of the MRI flexible imaging coil. Second, the aiming device is designed to be rigidly affixed to the support board. The base supporting board is affixed to the MRI scanner by using the 3D-printed trapezoidal block slides along the slots at the side of MRI bed. The skull is kept immobilized with respect to the aiming device by using the set screw (shown in Fig. 2c). Third, the aiming device is fabricated with plastic and acrylic materials, which ensures the robot safety and compatibility inside the scanner.

According to the aforementioned scanner bore size and average head circumference (≈ 550 mm) [23], the radius of the aiming device is chosen to be 100 mm, which provides sufficient safety margin as well as the space for flexible coil placement. The height of the vertical bar is chosen to be 80 mm, which assures that the remote center of motion of the aiming device is approximately located at the center of the skull. The aiming device is constructed with rapid
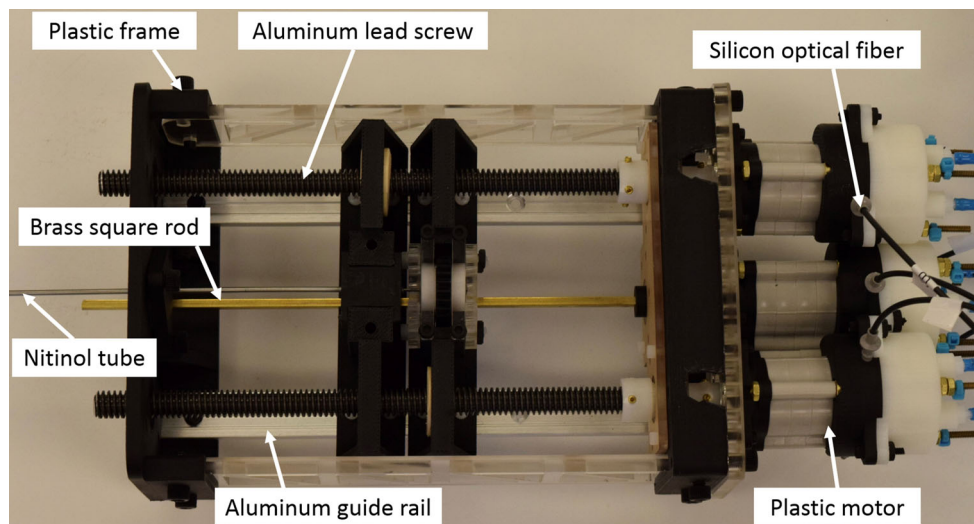
Fig. 3 MR-conditional ICH robot assembly

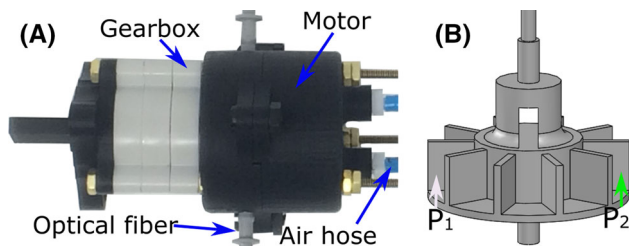**Fig. 4 a** Custom-designed MR-conditional pneumatic motor with optical encoder. The motor is coupled with a 100:1 gearbox, **b** 3D drawing of the rotor. Motor rotation direction is controlled by pressurized flow directed onto the turbine blades

prototyping, e.g., 3D printing (Stratasys Dimension SST, resolution: 0.254 mm) and a laser cutter (Kern laser cutting system). The arc was fabricated using acrylic material with the thickness of 6.35 mm. The two arcs were connected with a 3D-printed connector with ≈ 10 mm spacing which facilitates the deployment of the concentric tube through this gap. The protractor on the arc and vertical bar are engraved using a laser cutter with the resolution of $1°$ so that the aiming process can be carried out accurately. Three MRI fiducial markers are placed at predefined positions on the vertical bar to register the MR coordinate to the robot coordinates (as indicated in Fig. 2c).

MR-conditional ICH robot design

The proposed MR-conditional ICH robot prototype can be seen in Fig. 3. The 3-DoF ICH robot controls 2 tubes, which are the straight outer tube and the pre-curved aspiration inner tube made of superelastic nitinol. Both tubes can be inserted or retracted through lead screw mechanisms coupled with

the linear guiding rail. The rotational DoF of inner tube is achieved by using a square rod connected to the gear train. To ensure MR-conditionality, the lead screws are constructed with aluminum and the square shaft is fabricated with brass. The detailed description of the robot design and working principle can be found in [5, 21].

In order to function safely inside the MR room, all the components of the robot were fabricated or chosen from MR-conditional materials (e.g., aluminum, plastic, and brass). The high strength magnetic field inside the MRI scanner precludes the application of common electromagnetic motors. Hence, we utilize custom-designed pneumatic motors with built-in optical encoders [24] (Fig. 4). The motor control loop can be closed with the optical encoder feedback. A benefit from the compact motor design (Φ 40 mm $\times$ 70 mm) is that the total dimension of MR-conditional ICH robot is further reduced to ≈ 250 mm $\times$ 140 mm $\times$ 70 mm. Detailed motor characterization results show that the custom-designed pneumatic motor is able to achieve 460 mN m stall torque and 370 rpm no-load speed when coupled with a 100:1 gearbox [24]. The proposed pneumatic motor and encoder hardware satisfy the MR-conditionality requirement according to the ASTM F2503 standard [22].

Kinematic modeling

The aiming device is a 2RR mechanism and concentric on the origin of the supporting board, which is rotating around the pivot of the vertical bar (about the z-axis) and the slider rotating on the arc, respectively (Fig. 2). Let the homogeneous transformation (HT) that maps the MRI coordinate frame, $\{O_M\}$, to supporting board coordinate frame, $\{O_B\}$,

be $T_M \in SE(3)$, and this is found through the rigid registration method discussed in "Envisioned real-time MRI-guided surgical workflow" section. R_x and R_z are the basic rotation matrix around the x-axis and z-axis, respectively.

$$R_x = \begin{bmatrix} 1 & 0 & 0 \\ 0 & \cos(\theta) & -\sin(\theta) \\ 0 & \sin(\theta) & \cos(\theta) \end{bmatrix}, \quad R_z = \begin{bmatrix} \cos(\theta) & -\sin(\theta) & 0 \\ \sin(\theta) & \cos(\theta) & 0 \\ 0 & 0 & 1 \end{bmatrix}$$

Based on the kinematic relationship described in Fig. 5a, the rotation matrix of the slider frame, that mounts the concentric tube robotic system $\{O_R\}$, with respect to $\{O_B\}$ is $R_B \in SE(3)$ is given by

$$R_B^R = R_z(\theta) R_x(-\beta) \tag{1}$$

where $\theta \in \left[\frac{\pi}{4}, \frac{\pi}{2}\right]$ with respect to the z-axis, $\beta \in \left[-\frac{\pi}{3}, \frac{\pi}{3}\right]$ with respect to the x-axis. r is the radius of the 2RR mechanism from the origin of $\{O_B\}$, then the slider position after rotation inside the $\{O_B\}$ can be written in the following equation

$$P^B = R_B^R * \begin{bmatrix} 0 & 0 & -r \end{bmatrix}^T \tag{1}$$

The forward kinematics (Fig. 5b) of the concentric tube robot can be derived as $T_{\text{base}}^{\text{tip}} = T_\alpha T_R^{\text{tip}}$, where

$$T_\alpha = \begin{bmatrix} \cos(\alpha) & -\sin(\alpha) & 0 & 0 \\ \sin(\alpha) & \cos(\alpha) & 0 & 0 \\ 0 & 0 & 1 & 0 \\ 0 & 0 & 0 & 1 \end{bmatrix},$$

$$T_R^{\text{tip}} = \begin{bmatrix} 1 & 0 & 0 & 0 \\ 0 & \cos(\kappa_3 l_3) & -\sin(\kappa_3 l_3) & (\cos(\kappa_3 l_3) - 1)/\kappa_3 \\ 0 & \sin(\kappa_3 l_3) & \cos(\kappa_3 l_3) & (\cos(\kappa_3 l_3) - 1)/\kappa_3 \\ 0 & 0 & 0 & 0 \end{bmatrix} \tag{2}$$

where $\alpha \in [0, 2\pi]$ is the rotation angle of the inner tube with respect to the z-axis of slider, l_3 is the extension length of the curved tube, and κ_3 is the curvature of the curved tube.

The HT that maps the concentric tube robot base to the slider can be written as

$$T_{\text{slider}}^{\text{base}} = \begin{bmatrix} 1 & 0 & 0 & 0 \\ 0 & 1 & 0 & 0 \\ 0 & 0 & 1 & l_2 \\ 0 & 0 & 0 & 1 \end{bmatrix} \tag{3}$$

where l_2 is the outer tube extension length. Combining Eqs. 1–3 together, the mapping (T_{robot}) between the concentric tube robot tip to the aiming device can be obtained through the kinematic chain rule.

Inverse kinematics can be obtained through the resolved rates methods [25]. For a target position located inside the
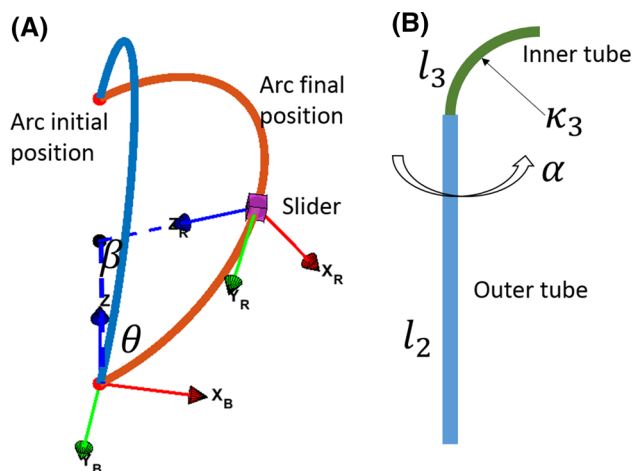

Fig. 5 a Kinematic relationship of the aiming device, b concentric tube robot kinematics based on the constant curvature assumption

MR coordinate frame, the joint values can be found through the following equation

$$q_i = q_{i-1} + \dot{q}_{\text{des}} * \Delta t \tag{4}$$

where Δt is the time step, and $\dot{q}_{\text{des}} = J^{-1} \dot{x}_{\text{des}}$. The robot jacobian J can be solved through the numerical perturbation method.

Experimental setup

All experiments were performed on a 3 Tesla Achieva MRI scanner (Philips Healthcare, Best, Netherlands). The experimental setup involves the MR-conditional ICH robot system, pneumatic valves (Festo MPYE-5-M5-010-B), data acquisition card (National Instruments PCI-6703), air supply (0.5 MPa) and vacuum pump (0.069 MPa). The experimental schematic diagram can be seen in Fig. 6. The robot control algorithm is implemented in MATLAB/Simulink and loaded onto a Simulink Realtime Target machine. The data acquisition card sends the control commands to the pneumatic valves at 1 kHz to regulate the air flow rate supplied to the air motors. A 32-bit pulse counter (Contec CNT32-8M) is applied to process the optical encoder signal. In the MR experiments, the robot is placed inside MRI machine and connected to the control electronics located in the MRI control room with three pairs of 8 m polyurethane air hose (OD 4 mm) and optical fibers. In addition, an air hose is used to channel the vacuum supply from the vacuum pump to the aspiration tube. With the real-time image feedback, the surgeon controls the ICH robot remotely through a custom-designed graphical user interface.
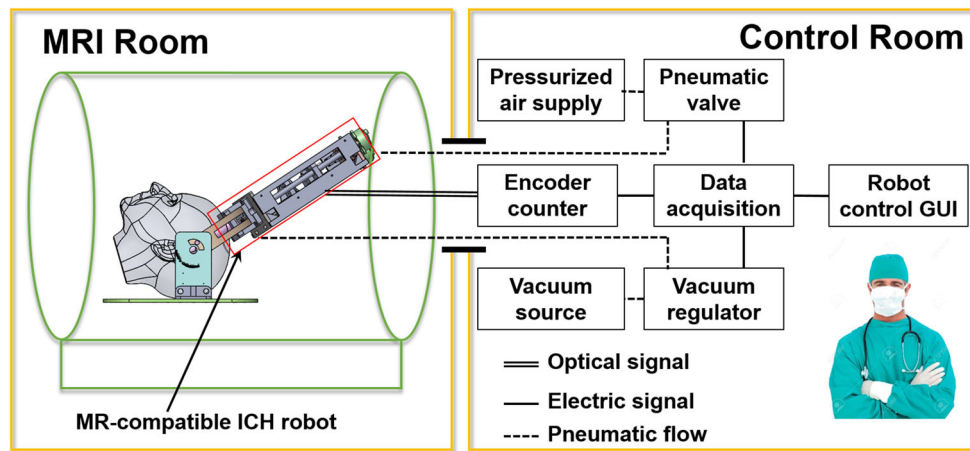
Fig. 6 Schematic diagram of the experimental setup inside an MR scanner

Envisioned real-time MRI-guided surgical workflow

Figure 7 shows the envisioned robotic based surgical workflow, which consists of the following two major steps: preoperative planning and preparation, and MR-guided intraoperative procedure. A high-resolution MR scanning is required prior to the surgery to localize the hematoma zone and identify the optimal treatment plan. Preoperative preparation includes patient anesthesia, affixation, needle insertion, burr hole creation, and dura opening, which is identical to the conventional MR-guided neurosurgeries [26]. Intraoperative procedure includes the robot-MRI coordinate frame registration, robot inverse kinematics calculation, tube deployment with MR guidance, and MR-guided ICH evacuation. Registration between MR coordinate frame and ICH robot system is performed with the rigid registration method [27], which can be written in the following equation.

$$P_{\text{Robot}} = R * P_{\text{MRI}} + d \tag{5}$$

where P_{Robot} is the fiducial marker position in the robot coordinate frame, P_{MRI} is the corresponding fiducial marker position in the MRI coordinate frame measured using 3D scout images, and R and d are the rotation and translation matrix, respectively. The fiducial marker registration error (FRE) is defined as the following equation

$$\text{FRE}^2 = \frac{1}{n} \sum_{i=1}^{n} \left| R P_{\text{MRI}\_i} + d - P_{\text{Robot}\_i} \right|^2 \tag{6}$$

where n is the number of fiducial markers. Three fiducial markers (PinPoint, Beekley Medical, Connecticut, USA) were used to perform the MRI-robot coordinate frame registration. Note that placing all the fiducial markers on the same line should be avoided in order to obtain the valid value of

R and d. In this study, these three fiducial markers were precisely placed on vertices of a right triangle engraved in the vertical supporting bar (see Fig. 2c). The HT can be calculated once the MR scan of the fiducial markers is obtained. The fiducial marker registration error (FRE) was 0.5 mm.

Having decided the best entry path to reach the hematoma, ICH robot is manipulated along the desired entry pose through an aiming device. Then the concentric tube is inserted by surgeon remote control through the burr hole to the hematoma under real-time MRI feedback guidance. Surgeon controls the needle insertion process by sending the command to the robot control computer through a custom-designed graphical user interface (GUI) written in MATLAB. Real-time MR image will be streamed to the custom-designed GUI through the MatMRI to provide image feedback [28]. The hematoma is aspirated through the precurved inner tube with real-time imaging of the hematoma site, which enables accurately monitoring of the hematoma boundary to maintain surgical safety. In addition, the image feedback also provides the intraoperative treatment outcome evaluation. High-resolution 3D scanning of the hematoma will be performed in the end of the procedure to further evaluate total evacuated volume.

Results

MR-conditionality evaluation

The MR-conditionality performance index can be evaluated by quantifying image artifacts and SNR variation of the region of interest (ROI) caused by the introduction of robot [29, 30]. In this experiment, we take the images of a bottle filled with CuSO4 [31] as the ROI. The experiment was performed in three scenarios, namely (1) without the robot, (2)
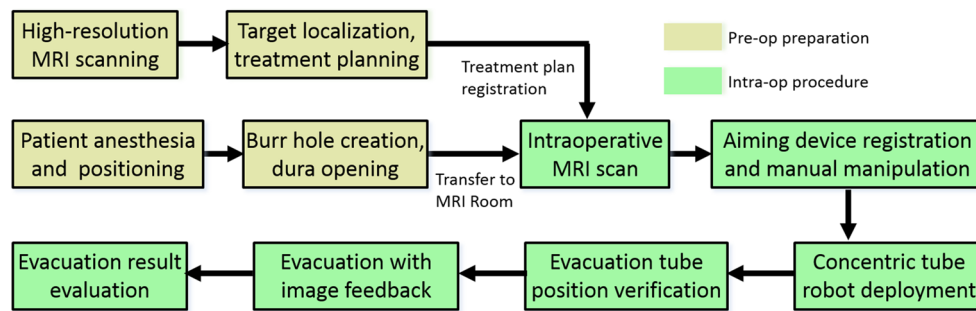
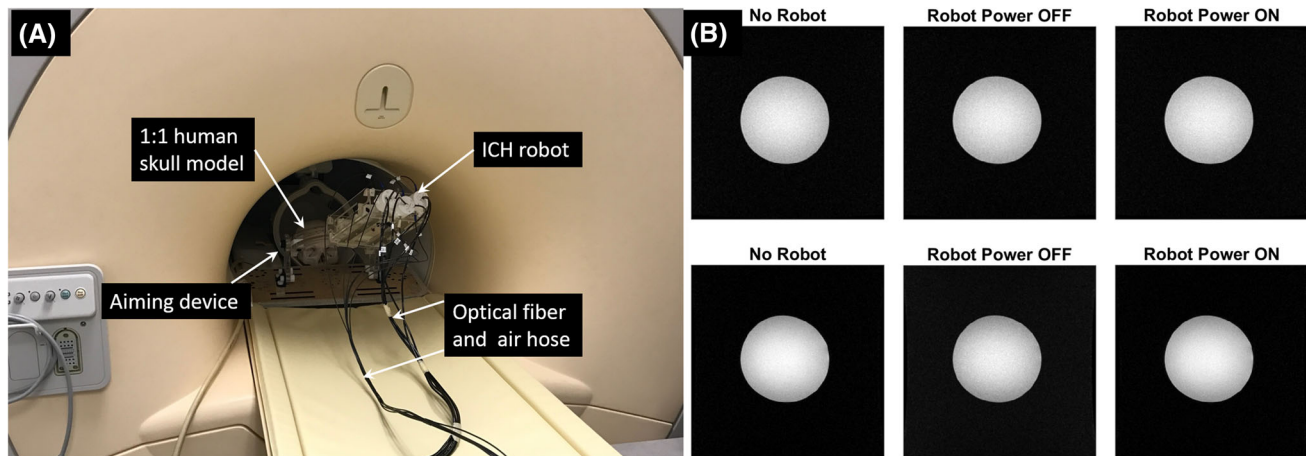**Fig. 7** Envisioned workflow for MR-guided ICH removal

Fig. 8 **a** In-scanner experimental setup of the proposed ICH robot, **b** MR-conditionality test result. T1-weighted (1st row) and T2-weighted (2nd row) MR phantom images obtained when the robot is not in the scanner, robot powered off and powered on in a 3T Philips MR scanner

with the robot powered off, and (3) with the robot powered and running. In the latter two scenarios, the needle tip was placed next to the phantom bottle at a distance less than 5 mm, where the ICH phantom model was located at the isocenter of the MRI scanner. The detailed experimental setup can be seen in Fig. 8a. Both T1-weighted fast field echo (T1W-FFE) and T2-weighted turbo spin echo (T2W-TSE) protocols were applied to obtain the phantom bottle image. The ROI was selected in the coronal plane and at the same level of the outer tube axis in the Y-direction of MR coordinate frame. An artifact can be defined as 30% pixel intensity change within the ROI image [31]. In Fig. 8b, no image artifacts were observed when the needle tip and the ICH robot system motor were introduced to the scanner space in both imaging protocols. SNR is calculated from μ/σ, where μ is the mean image intensity within the 40×40 pixel region at the center of the image and σ is the standard deviation of the image intensity at the corner of the 40×40 pixel region. The maximum SNR reduction is 3.2% and 4.9% for T1W-FFE and T2W-TSE images, respectively, which were within the acceptable range for devices used inside the MR room.

Robot targeting accuracy

The ICH robot's targeting accuracy was evaluated in a set of bench-top experiments using an electromagnetic tracking system. In this study, we used an Aurora system (Northern Digital, Inc.) and its 6-DoF probe sensor (0.48 mm) to perform the targeting accuracy validation experiment. The robot coordinate frame was registered to the tracker coordinate frame through the point-based registration method [27]. Targeting test was performed by (1) selecting a point within the robot workspace, (2) calculating the robot joint motion through the inverse kinematics, (3) deploying the needle to the desired position, and (4) quantifying the targeting error. The error is defined as the Euclidean distance between the desired tip positions and actual tip positions. During each targeting test, the desired target positions were randomly selected within the robot workspace with the outer tube insertion depth ranges from 50 mm to 200 mm. A total of 38 needle tip position measurements were obtained and compared. The robot had an overall targeting accuracy of 1.26 ± 1.22 mm (Fig. 9), which is within the acceptable range according to the feedback of our clinical collaborators.
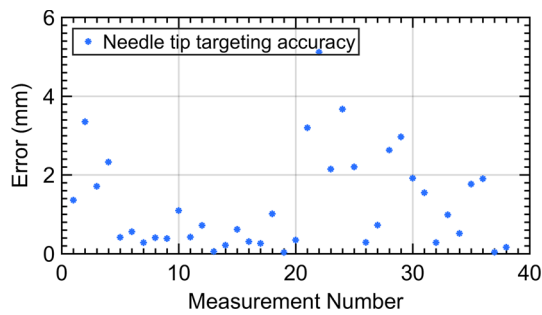
Fig. 9 Robot targeting error in free space evaluation

Real-time MR-guided needle insertion

Figure 10 shows the process of remotely steering the needle of the ICH robot by a surgeon into a gelatin ICH model under real-time MRI guidance. The needle insertion path planning in the experimental study was performed by (1) selecting the target point by the surgeon and (2) calculating the robot joint space motion according to the method presented in "Kinematic modeling" section. The target point was selected by the surgeon in this experiment, which was approximately in the center of the lower circle. Prior to insertion, the robot inverse kinematics model was used to verify whether the target point was located within the needle workspace [5]. Gradient recalled echo (GRE) imaging protocol (FOV: 240 mm × 240 mm, resolution: 1 mm × 1 mm, slice thickness: 4 mm, flip angle: 15°, TR: 8.6 ms, TE: 1.58 ms, update rate: 1.8 Hz) was selected in the experimental study to provide the real-time image guidance.

To mimic the clinical implementations, the full needle insertion procedure was divided into multiple discrete steps by the surgeon (as can be seen in different subplots of Fig. 10). Based on the feedback of our clinical collaborators, this multiple-step insertion procedure is also preferred in clinical scenarios to avoid large insertion errors at the needle tip. Employing the multistep approach and real-time monitoring of the insertion process, the surgeon took 99.4 s to reach the target (total insertion distance = 38 mm). Based on the surgeon's post-operative evaluation, the needle successfully reached the desired target position with a promising confidence level. With real-time MRI guidance, the control loop was closed through the continuous intraoperative needle image feedback. Hence, targeting error under real-time MRI guidance is only dependent on the surgeon's experience.

In this preliminary study, the outer straight tube insertion can be monitored in the real-time imaging by aligning the imaging plane that contains the linear insertion trajectory. To obtain the images during needle steering, the imaging plane has to be dynamically updated to ensure that the curved needle is always located inside the field of view regardless of its steering direction and speed. To achieve this goal, a set of micro RF coils will be non-collinearly mounted on the curved needles to provide the high-resolution position feedback (update rate: 30 Hz [13]). The updated imaging plane can be determined by the RF coil position feedback.

MR-guided ICH evacuation: phantom study

A phantom experiment was performed to evaluate the performance of robotic ICH evacuation under real-time MRI guidance. The outer tube has the outer diameter of 3.5 mm and inner diameter of 2.5 mm. The aspiration tube has the outer diameter of 2.2 mm and inner diameter of 1.5 mm. The radius of curved portion is 20 mm and the length is 27.5 mm.

Fig. 10 Real-time MRI-guided needle insertion. Six frames of the total insertion process are shown here. The blue point indicates the target position selected by the surgeon
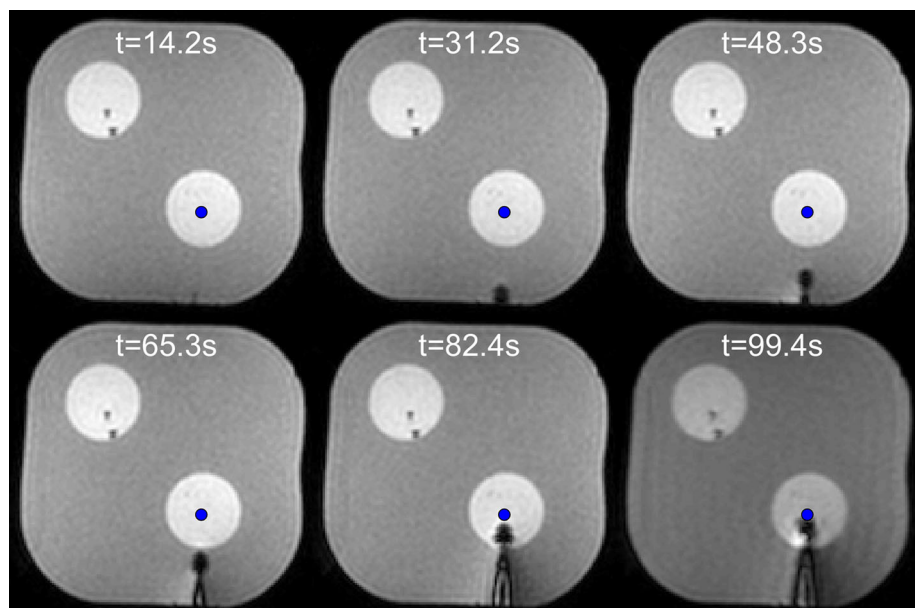
Fig. 11 a Schematic diagram of the phantom with elastic properties. **b** Gelatin phantom for MR-guided aspiration test. The red square indicates the low-density soft gelatin phantom. The blue dashed square indicates the entry window for the concentric tube
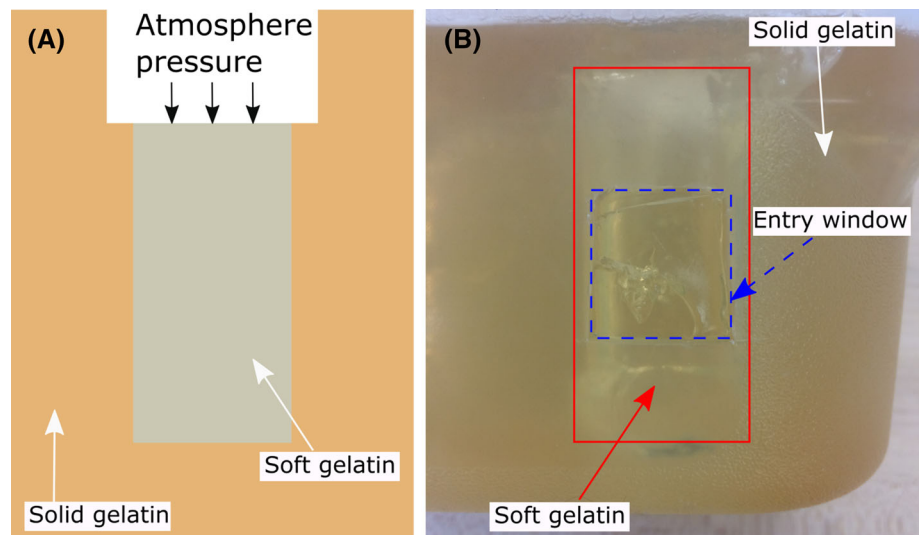

Fig. 12 Phantom experiment demonstrates hemorrhage clot evacuation with the proposed MR-conditional ICH robotic system. The dark point on each figure indicates the aspiration tube tip position. The height of soft gelatin is labeled with the white lines. Evacuation is performed at $t = 6.8$ s; from 111.3 to 155.1 s, surgeon monitors the intraoperative surgical outcome, and hence, the height is constant; the inner tube breaks the gel phantom from 155.1 to 159.6 s; the aspiration is continued to the end of the experiment
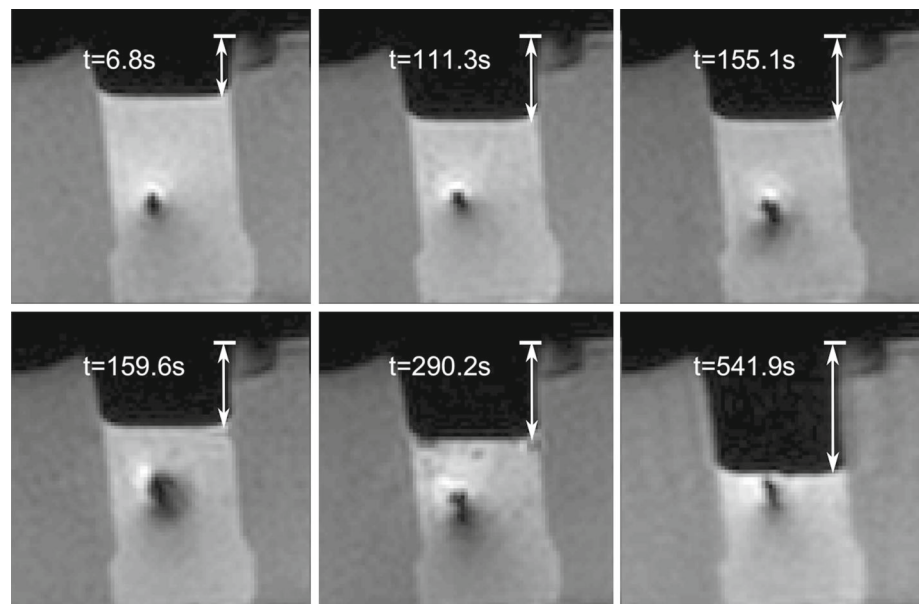
Tubes are made of nitinol to ensure MR compatibility. Needle insertion was controlled by a surgeon remotely from the control room under real-time MRI guidance. Once within the ICH, the aspiration tube extends from the outer tube to evacuate the soft phantom clot.

Intraoperative brain deformation due to the pressure variation is a common phenomenon in neurosurgical procedures. The hematoma-brain tissue boundary collapses as the hematoma is evacuated. To mimic this phenomenon, we used the gelatin phantom (Fig. 11) with two different densities in the experimental study. Both atmospheric pressure and gravity force contribute to the soft gel phantom collapse when aspiration starts. Over-evacuation of the surrounding

healthy tissues happens when the upper surface of soft gelatin is lower than the needle insertion point.

Figure 12 shows the exemplary slices during the aspiration process under real-time MR guidance (same imaging protocol as "Real-time MR-guided needle insertion" section were employed). It can be seen that the height of the low-density gelatin phantom (ICH model) gradually reduces during the aspiration. Note that the height was constant from $t = 111.3$ s to $t = 155.1$ s while the surgeon was evaluating the intraoperative aspiration outcome. The aspiration procedure stopped at $t = 541.9$ s when the surgeon believed that a significant amount of ICH was evacuated. The surgeon did not evacuate the whole ICH model in the phantom study since it is believed that 25–50% evacuation could lead to the positive

clinical results [5]. The experiment lasted for approximately 9 min during which 11.3 ml of the ICH model was aspirated, which is 58.8% of total ICH model. Neither over-evacuation nor the tip entering into the surrounding tissue was observed throughout the experiment.

Discussion

ICH is one of the deadliest forms of stroke in the USA with a 30-day mortality rate of 43%. Conventional surgical techniques such as craniotomy or stereotactic aspiration disrupt a large volume of healthy brain tissue in their attempts to reach the target. Concentric tube robots have been shown to be able to reach the target through a needle-sized entry path with less damage to the healthy tissue.

In this paper, we proposed a real-time MRI-guided robotic system to address the imaging limitations of current methods. We have described the design requirements and working principles of the aiming mechanism, ICH concentric tube robot. The robot's forward and inverse kinematics are discussed in the paper. Needle insertion experimental results demonstrated that the robot has a targeting accuracy of 1.26 ± 1.22 mm in the bench-top testing environment. MR-conditionality tests indicated that the robot could operate safely inside a 3T MRI scanner without inducing image artifacts at the region of interests. In addition, the robotic system has shown to be MR-conditional with a small SNR variation (maximum reduction was 4.9%). Real-time MRI-guided targeting tests indicated that the proposed robotic system could accurately reach the desired position by closing the control loop through the image feedback. ICH evacuation in a gelatin phantom model using real-time MR imaging feedback showed that the hematoma can be accurately, efficiently and safely aspirated (11.3 ml in 9 min) without significantly disrupting surrounding tissue. This is the first time a concentric tube robotic system has been integrated with real-time MR image feedback and experimentally validated in phantom studies for ICH treatment. The robotic system has the potential to facilitate accurate, safe and efficient targeting and aspiration, which could improve the post-stroke quality of life and reduce total health-care costs.

Future work will focus on (1) optimization of the robotic system, (2) integrating the micro MR active tracking technique to achieve the real-time imaging of steering motion, (3) rigorous feasibility evaluation of the proposed robotic system, especially in learning curve evaluation, the ex vivo and in vivo tissue experiment, and (4) further evaluation of MR-guided robotic ICH evacuation performance in cadaver studies.

Compliance with ethical standards

Conflict of interest The authors declare that they have no conflict of interest.

Ethical approval This article does not contain any studies with human participants or animals performed by any of the authors.

Informed consent This article does not contain patient data.

References

1. Tapia-Perez JH, Zilke R, Schneider T (2016) Match-study of statin therapy in spontaneous intracerebral hemorrhage: is the discontinuation reasonable? J Neurosurg Sci 60:301–312
2. Etminan N, Beseoglu K, Turowski B, Steiger H-J, Hänggi D (2012) Perfusion CT in patients with spontaneous lobar intracerebral hemorrhage: effect of surgery on perihemorrhagic perfusion. Stroke 43:759–763
3. Elijovich L, Patel PV, Hemphill JC (2008) Intracerebral hemorrhage. Semin Neurol 28(5):657–667
4. Maira G, Anile C, Colosimo C, Rossi GF (2002) Surgical treatment of primary supratentorial intracerebral hemorrhage in stuporous and comatose patients. Neurol Res 24:54–60
5. Burgner J, Swaney PJ, Lathrop RA, Weaver KD, Webster RJ (2013) Debulking from within: a robotic steerable cannula for intracerebral hemorrhage evacuation. IEEE Trans Biomed Eng 60:2567–2575
6. Granna J, Godage IS, Wirz R, Weaver KD, Webster RJ, Burgner-Kahrs J (2016) A 3-D volume coverage path planning algorithm with application to intracerebral hemorrhage evacuation. IEEE Robot Autom Lett 1:876–883
7. Godage IS, Remirez AA, Wirz R, Weaver KD, Burgner-Kahrs J, Webster RJ (2015) Robotic intracerebral hemorrhage evacuation: an in-scanner approach with concentric tube robots. In: 2015 IEEE/RSJ international conference on intelligent robots and systems (IROS), 2015, pp 1447–1452
8. Miga MI, Paulsen KD, Hoopes PJ, Kennedy FE, Hartov A, Roberts DW (2000) In vivo quantification of a homogeneous brain deformation model for updating preoperative images during surgery. IEEE Trans Biomed Eng 47:266–273
9. Fiebach JB, Schellinger PD, Gass A, Kucinski T, Siebler M, Villringer A, Ölkers P, Hirsch JG, Heiland S, Wilde P (2004) Stroke magnetic resonance imaging is accurate in hyperacute intracerebral hemorrhage: a multicenter study on the validity of stroke imaging. Stroke 35:502–506
10. Jolesz FA (2003) Future perspectives in intraoperative imaging. In: Bernays RL, Imhof HG, Yonekawa Y (eds) Intraoperative Imaging in Neurosurgery, vol 85. Springer, Vienna, pp 7–13
11. Sengupta S, Tadanki S, Gore JC, Welch EB (2014) Prospective real-time head motion correction using inductively coupled wireless NMR probes. Magn Reson Med 72:971–985
12. Wang W, Viswanathan AN, Damato AL, Chen Y, Tse Z, Pan L, Tokuda J, Seethamraju RT, Dumoulin CL, Schmidt EJ (2015) Evaluation of an active magnetic resonance tracking system for interstitial brachytherapy. Med Phys 42:7114–7121
13. Chen Y, Wang W, Schmidt EJ, Kwok K-W, Viswanathan AN, Cormack R, Tse ZTH (2016) Design and fabrication of MR-tracked metallic stylet for gynecologic brachytherapy. IEEE/ASME Trans Mechatron 21:956–962

14. Kwok K-W, Lee K-H, Chen Y, Wang W, Hu Y, Chow GC, Zhang HS, Stevenson WG, Kwong RY, Luk W (2014) Interfacing fast multi-phase cardiac image registration with MRI-based catheter tracking for MRI-guided electrophysiological ablative procedures. Am Heart Assoc, Dallas

15. Kwok K-W, Chen Y, Chau TC, Luk W, Nilsson KR, Schmidt EJ, Zion TT (2014) MRI-based visual and haptic catheter feedback: simulating a novel system's contribution to efficient and safe MRI-guided cardiac electrophysiology procedures. J Cardiovasc Magn Reson 16:O50

16. Chen Y, Zion TT, Wang W, Kwong RY, Stevenson WG, Schmidt EJ (2015) Intra-cardiac MR imaging and MR-tracking catheter for improved MR-guided EP. J Cardiovasc Magn Reson 17:P237

17. Masamune K, Kobayashi E, Masutani Y, Suzuki M, Dohi T, Iseki H, Takakura K (1995) Development of an MRI-compatible needle insertion manipulator for stereotactic neurosurgery. J Image Guided Surg 1:242–248

18. Pandya S, Motkoski JW, Serrano-Almeida C, Greer AD, Latour I, Sutherland GR (2009) Advancing neurosurgery with image-guided robotics. J Neurosurg 111:1141–1149

19. Sheng J, Desai JP (2015) Towards a SMA-actuated neurosurgical intracerebral hemorrhage evacuation (NICHE) robot. In: 2015 IEEE/RSJ international conference on intelligent robots and systems (IROS), pp 3805–3810

20. Su H, Li G, Rucker DC, Webster RJ III, Fischer GS (2016) A concentric tube continuum robot with piezoelectric actuation for MRI-guided closed-loop targeting. Ann Biomed Eng 44:2863–2873

21. Chen Y, Godage IS, Sengupta S, Liu CL, Weaver KD, Barth EJ, Webster RJ (2017) An MRI-compatible robot for intracerebral hemorrhage removal. In: 2017 design of medical devices conference, pp V001T08A019–V001T08A019

22. ASTM. F2503 (2005) Standard practice for marking medical devices and other items for safety in the magnetic resonance environment. http://www.astm.org/. Accessed 21 Jan 2018

23. Bushby K, Cole T, Matthews J, Goodship J (1992) Centiles for adult head circumference. Arch Dis Child 67:1286–1287

24. Chen Y, Godage IS, Tse ZTH, Webster RJ, Barth EJ (2017) Characterization and control of a pneumatic motor for MR-conditional robotic applications. IEEE/ASME Trans Mechatron 22:2780–2789

25. Whitney DE (1969) Resolved motion rate control of manipulators and human prostheses. IEEE Trans Man Mach Syst 10:47–53

26. Chan AY, Tran DKT, Gill AS, Hsu FP, Vadera S (2016) Stereotactic robot-assisted MRI-guided laser thermal ablation of radiation necrosis in the posterior cranial fossa. Neurosurg Focus 41:E5

27. Fitzpatrick JM, West JB, Maurer CR Jr (1998) Predicting error in rigid-body point-based registration. IEEE Trans Med Imaging 17:694–702

28. Sinclair T, Mougenot C, Kivinen J (2012) MatMRI and MatHIFU: Matlab toolboxes for real-time monitoring and control of MR-HIFU. In: 12th international society for therapeutic ultrasound symposium, Heidelberg, Germany, pp 156–161

29. Chen Y, Kwok K-W, Tse ZTH (2014) An MR-conditional high-torque pneumatic stepper motor for MRI-guided and robot-assisted intervention. Ann Biomed Eng 42:1823–1833

30. Chen Y, Mershon CD, Tse ZTH (2015) A 10-mm MR-conditional unidirectional pneumatic stepper motor. IEEE/ASME Trans Mechatron 20:782–788

31. Chen Y, Squires A, Seifabadi R, Xu S, Agarwal HK, Bernardo M, Pinto PA, Choyke P, Wood B, Tse ZTH (2017) Robotic system for MRI-guided focal laser ablation in the prostate. IEEE/ASME Trans Mechatron 22:107–114